Article

Superconductivity in pressurized trilayer $La_4Ni_3O_{10-\delta}$ single crystals

https://doi.org/10.1038/s41586-024-07553-3

Received: 13 November 2023

Accepted: 9 May 2024

Published online: 17 July 2024

Check for updates

Yinghao Zhu[1,2,13], Di Peng[3,13], Enkang Zhang[1,13], Bingying Pan[4,13], Xu Chen[5,13], Lixing Chen[1], Huifen Ren[5], Feiyang Liu[1], Yiqing Hao[6], Nana Li[7], Zhenfang Xing[7], Fujun Lan[7], Jiyuan Han[1], Junjie Wang[5,8], Donghan Jia[9], Hongliang Wo[1], Yiqing Gu[1], Yimeng Gu[1], Li Ji[10], Wenbin Wang[11], Huiyang Gou[9], Yao Shen[5], Tianping Ying[5], Xiaolong Chen[5], Wenge Yang[7], Huibo Cao[6], Changlin Zheng[1], Qiaoshi Zeng[3,7] ✉, Jian-gang Guo[5] ✉ & Jun Zhao[1,2,11,12] ✉

The pursuit of discovering new high-temperature superconductors that diverge from the copper-based model[1–3] has profound implications for explaining mechanisms behind superconductivity and may also enable new applications[4–8]. Here our investigation shows that the application of pressure effectively suppresses the spin–charge order in trilayer nickelate $La_4Ni_3O_{10-\delta}$ single crystals, leading to the emergence of superconductivity with a maximum critical temperature (T_c) of around 30 K at 69.0 GPa. The d.c. susceptibility measurements confirm a substantial diamagnetic response below T_c, indicating the presence of bulk superconductivity with a volume fraction exceeding 80%. In the normal state, we observe a strange metal behaviour, characterized by a linear temperature-dependent resistance extending up to 300 K. Furthermore, the layer-dependent superconductivity observed hints at a unique interlayer coupling mechanism specific to nickelates, setting them apart from cuprates in this regard. Our findings provide crucial insights into the fundamental mechanisms underpinning superconductivity, while also introducing a new material platform to explore the intricate interplay between the spin–charge order, flat band structures, interlayer coupling, strange metal behaviour and high-temperature superconductivity.

Cuprates are the first family of high-temperature (high-T_c) superconducting materials, characterized by layers of CuO_2 interleaved with charge reservoir layers[1,2]. Despite intensive research on various cuprates, the mechanism responsible for high-T_c superconductivity remains unknown[2,3]. Consequently, the pursuit of high-T_c superconductors that do not rely on copper oxides has become a focal point of intense experimental and theoretical exploration since the discovery of cuprates nearly four decades ago[4–8]. This is motivated by the belief that these materials may help to explain the enigmatic mechanisms governing high-T_c superconductivity while providing opportunities for new applications. Nickel, situated immediately to the left of copper on the Periodic Table, offers a playground for materials and chemistry designs aimed at replicating high-T_c unconventional superconductivity[8–12]. However, despite intensive efforts, achieving superconductivity in nickelates is a formidable challenge. In 2019, a development occurred when superconductivity was observed in infinite-layer nickelate thin films with T_c = 5–20 K (refs. 13–16). In these materials, Ni^{1+} (d^9) forms square planar NiO_2 layers closely resembling Cu^{2+} (d^9) in cuprates[13–16].

More recently, signatures of superconductivity have also been observed in the Ruddlesden–Popper bilayer perovskite $La_3Ni_2O_7$ under high pressure, achieving a T_c of approximately 80 K above 14 GPa (ref. 17). Subsequent studies have observed zero resistance under improved hydrostatic pressure conditions facilitated by a liquid pressure-transmitting medium[18–20]. However, it has been suggested that the superconductivity in $La_3Ni_2O_7$ may be filamentary in nature, with a low superconducting volume fraction[19,20], underscoring the need for more in-depth research to fully understand the superconducting properties of this class of materials. Unlike infinite-layer nickelates and cuprates with a d^9 electron configuration, $La_3Ni_2O_7$ hosts a bilayer NiO_2 square structure featuring $Ni^{2.5+}$ ($d^{7.5}$) ions[17]. Furthermore, the *p*-orbital of apical oxygen, which connects adjacent NiO_2 layers, couples the two nearest-neighbour $3d_{z^2}$ orbitals, suggesting that interlayer coupling may also play a crucial part in $La_3Ni_2O_7$ (ref. 17). However, in contrast to cuprate and iron-based superconductors, in which superconductivity typically arises from the suppression of static long-range magnetic order in their parent phases[2–4,21], infinite-layer and bilayer $La_3Ni_2O_7$ nickelates have either shown a lack

[1]State Key Laboratory of Surface Physics and Department of Physics, Fudan University, Shanghai, China. [2]Shanghai Research Center for Quantum Sciences, Shanghai, China. [3]Shanghai Key Laboratory of Material Frontiers Research in Extreme Environments (MFree), Institute for Shanghai Advanced Research in Physical Sciences (SHARPS), Shanghai, China. [4]College of Physics and Optoelectronic Engineering, Ocean University of China, Qingdao, China. [5]Beijing National Laboratory for Condensed Matter Physics, Institute of Physics, Chinese Academy of Sciences, Beijing, China. [6]Neutron Scattering Division, Oak Ridge National Laboratory, Oak Ridge, TN, USA. [7]Center for High Pressure Science and Technology Advanced Research, Shanghai, China. [8]School of Physical Sciences, University of Chinese Academy of Sciences, Beijing, China. [9]Center for High Pressure Science and Technology Advanced Research, Beijing, China. [10]State Key Laboratory of ASIC and System, School of Microelectronics, Fudan University, Shanghai, China. [11]Institute of Nanoelectronics and Quantum Computing, Fudan University, Shanghai, China. [12]Shanghai Branch, Hefei National Laboratory, Shanghai, China. [13]These authors contributed equally: Yinghao Zhu, Di Peng, Enkang Zhang, Bingying Pan, Xu Chen. ✉e-mail: zengqs@hpstar.ac.cn; jgguo@iphy.ac.cn; zhaoj@fudan.edu.cn

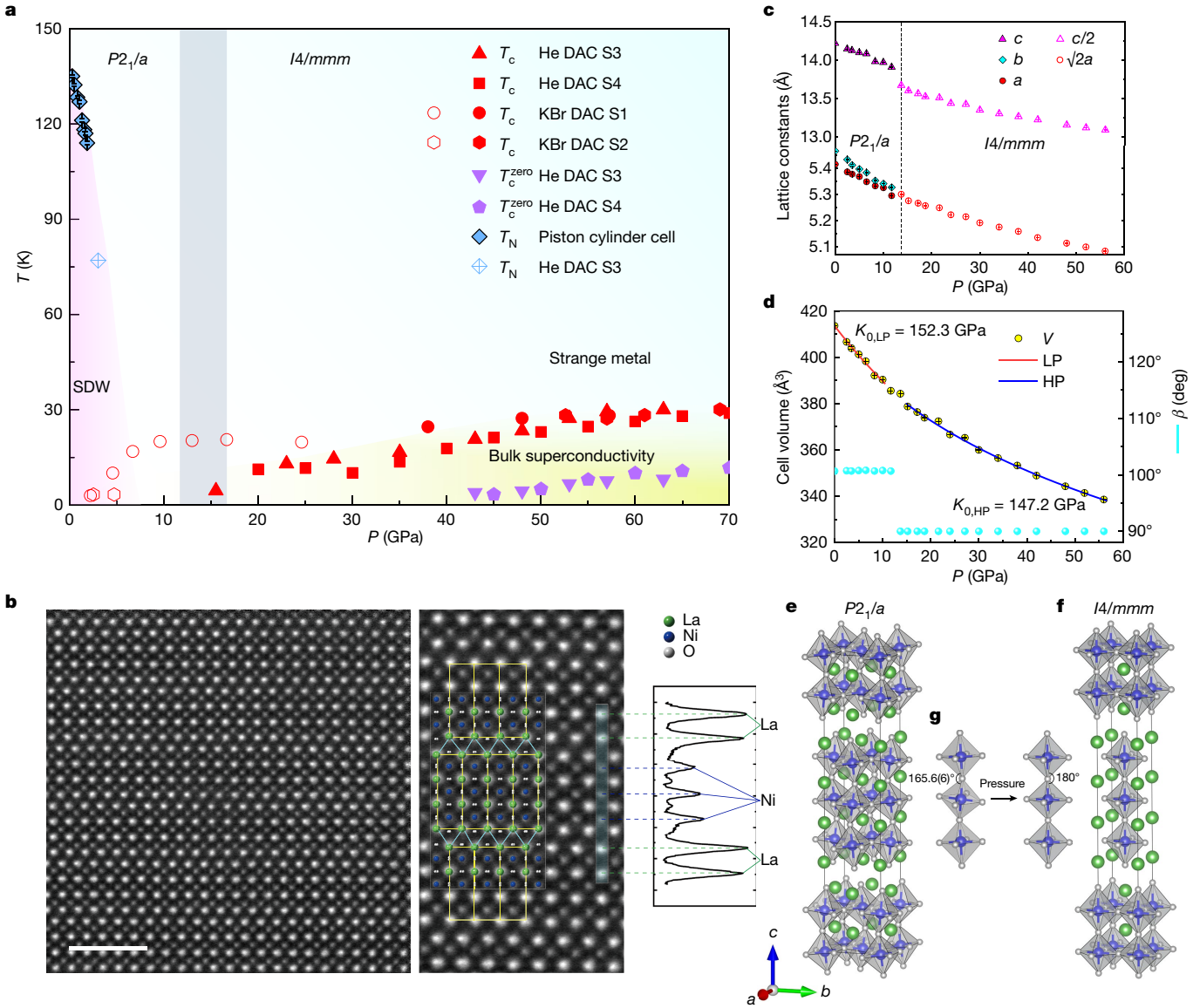

Fig. 1 | Pressure-dependent lattice structure and phase diagram of $La_4Ni_3O_{10-\delta}$. **a**, Phase diagram of $La_4Ni_3O_{10-\delta}$ under pressure. The red solid triangles and squares represent T_c (onset) of samples S3 and S4 in the helium DAC, respectively. The T_c (onset) is the temperature below which the resistance deviates from its linear dependence at high temperatures. The red solid circles and hexagons represent the T_c (onset) at pressures above 38 GPa of samples S1 and S2, respectively, in which a pronounced sharp drop in resistance below T_c is evident in the KBr DAC. The red open circles and hexagons denote the T_c (onset) at pressures below 25 GPa in the KBr DAC, in which a moderate decrease in resistance below T_c is observed because of filamentary superconductivity (Fig. 3e). The blue diamonds denote the T_N determined from resistance measurements in Fig. 3a,b and Supplementary Fig. 7. The purple solid downward triangles and pentagons represent the T_c offset T_c^{zero}, in which the resistance equals zero. The bulk superconductivity emerges above around 40 GPa, in which substantial superconducting diamagnetic responses and zero resistance are observed. The shaded area highlights the region of the structural transition. **b**, HAADF images along the [110] direction at ambient pressure, featuring three layers of NiO_2 separated by LaO spacers. **c**, Lattice constants *a*, *b* and *c* extracted from the synchrotron-based XRD (Extended Data Fig. 3). **d**, Cell volume *V* and the refined β angle of $P2_1/a$ and $I4/mmm$ lattices. The solid lines indicate the Birch–Murnaghan equation fit of cell volume as a function of pressure, with fitted bulk moduli K_0 of 152.3 GPa for the low-pressure phase and 147.2 GPa for the high-pressure phase. **e**, Crystal structure of $La_4Ni_3O_{10-\delta}$ at ambient pressure. **f**, Crystal structure of $La_4Ni_3O_{10-\delta}$ at 34 GPa. **g**, Evolution of Ni–O–Ni angle between adjacent NiO_2 layers across the structural phase transition. Error bars indicate 1 s.d. DAC, diamond anvil cell; LP, low pressure; HP, high pressure. Scale bar, 2 nm (**b**).

of magnetic order or hinted at the presence of weak magnetism[13,17,22,23]. This raises a fundamental question about whether magnetism plays the same crucial part in making nickelates into high-T_c superconductors.

Of particular interest, it is well known that the T_c in cuprates depends on the number of CuO_2 layers (n) in a non-monotonic way, reaching a maximum for $n = 3$ in most cases[24–26]. As a result, trilayer cuprates have the highest T_c among all cuprates, reaching up to 135 K at ambient pressure and 164 K under high pressure for mercury-based compounds[27,28]. The mechanism for this layer dependence of superconductivity remains a subject of intense and ongoing debate[26–30]. This raises the question of whether trilayer nickelates exhibit superconductivity, and if so, how it might influence T_c.

Theoretical considerations have suggested that trilayer $La_4Ni_3O_8$, with its $Ni^{1.33+}$ ($d^{8.67}$) configuration, closely parallels the cuprates with Cu^{2+}/Cu^{3+} configurations and thus stands as an ideal candidate for a high-T_c superconductor[31,32]. However, experimental investigations have thus far failed to observe superconductivity in trilayer $La_4Ni_3O_8$, both under ambient conditions and at high pressure[11,33].

In contrast to many nickelates that exhibit insulating behaviour, including trilayer $La_4Ni_3O_8$, the trilayer Ruddlesden–Popper compound

$La_4Ni_3O_{10}$ stands out as a rare oxide compound that maintains its metallic character even at low temperatures under ambient pressure[34,35]. Trilayer nickelate $La_4Ni_3O_{10}$ exhibits a static incommensurate magnetic order accompanied by a charge order[36]. The nominal valence state of trilayer $La_4Ni_3O_{10}$ is $Ni^{2.67+}$ ($d^{7.33}$), which is different from the d^9 state typically observed in infinite-layer nickelates and cuprates or the $d^{7.5}$ state found in bilayer $La_3Ni_2O_7$. Nevertheless, the band structure of $La_4Ni_3O_{10}$ shows intriguing features: the $d_{x^2-y^2}$ hole band bears a striking resemblance to the behaviour observed in hole-doped cuprates, whereas the d_{z^2} band is rather flat and exhibits a 20-meV density wave-like gap opening associated with the spin order transition[35,36], reminiscent of the phenomena observed in iron-based superconductors[21,37]. This distinctive combination of characteristics, coupled with its trilayer structure, positions $La_4Ni_3O_{10}$ as an ideal platform for the exploration of the interplay between magnetism, interlayer coupling and potential superconductivity. However, the investigations of $La_4Ni_3O_{10}$ were markedly hampered by the scarcity of high-quality single crystals, which necessitated their growth under a high oxygen pressure atmosphere[34].

In this study, we report detailed measurements of $La_4Ni_3O_{10-\delta}$ single crystals under both ambient conditions and high pressures, reaching up to 70 GPa. The high-quality $La_4Ni_3O_{10-\delta}$ single crystals were grown using a high-pressure vertical optical-image floating-zone furnace. Our X-ray diffraction (XRD) experiments conducted on powdered $La_4Ni_3O_{10-\delta}$ single crystals at ambient conditions confirm the presence of a pure phase of trilayer $La_4Ni_3O_{10-\delta}$ (Extended Data Fig. 1). Furthermore, we conducted single-crystal neutron-diffraction and single-crystal XRD measurements on $La_4Ni_3O_{10-\delta}$ (Extended Data Fig. 7a and Supplementary Table 1). The combined single-crystal structural refinement analysis using least square fitting by incorporating data from both neutron diffraction and XRD, identified the composition as $La_4Ni_3O_{9.96(4)}$, pointing to a minor oxygen deficiency. Moreover, the refined crystal structure aligns with the $P2_1/a$ space group with $Z = 2$ (Fig. 1e), consistent with previous reports[34].

Figure 1b shows the atomic-resolution high-angle annular dark-field (HAADF) images, which show the detailed positions of atoms within the trilayer structure of $La_4Ni_3O_{10-\delta}$. We also used integrated differential phase contrast (iDPC) imaging techniques to accurately visualize the lighter oxygen atoms (Extended Data Fig. 6). The simultaneous acquisition of HAADF and iDPC images, seamlessly aligns with our neutron diffraction and XRD refinements, reinforcing the accuracy of our structural analysis. The HAADF images in large-area overviews further confirm the phase purity and exceptional quality of our crystals (Extended Data Fig. 6).

To assess the influence of pressure on the crystal structure, we conducted synchrotron-based XRD measurements on powdered $La_4Ni_3O_{10-\delta}$ single crystals (Extended Data Fig. 3). It is shown that the diffraction peaks within the range of $12.5° < 2\theta < 14°$ exhibit a noticeable evolution with increasing pressure, indicative of a structural phase transition. The refinement analyses show a subtle structural transition associated with the tilting of the NiO_6 octahedra, shifting from monoclinic $P2_1/a$ to tetragonal $I4/mmm$ at pressures exceeding approximately 13–15 GPa (Extended Data Fig. 3). Concurrently, the Ni–O–Ni angle between adjacent NiO_2 layers changes from around 165.6(6)° to 180° during this phase transition (Fig. 1g), potentially enhancing interlayer coupling. The lattice constants and cell volume also exhibited a progressive decrease under pressure, with an anomaly observed near the structural phase transition (Fig. 1c,d), consistent with a recent independent measurement on polycrystalline samples[38]. To ascertain if such a phase transition also occurs in single-crystal samples, single-crystal XRD measurements were conducted, with the structural phase transition being further confirmed by single-crystal refinements (Extended Data Fig. 7b and Supplementary Table 2).

To further characterize the material, we conducted magnetic susceptibility measurements, which showed a distinct kink in the data at

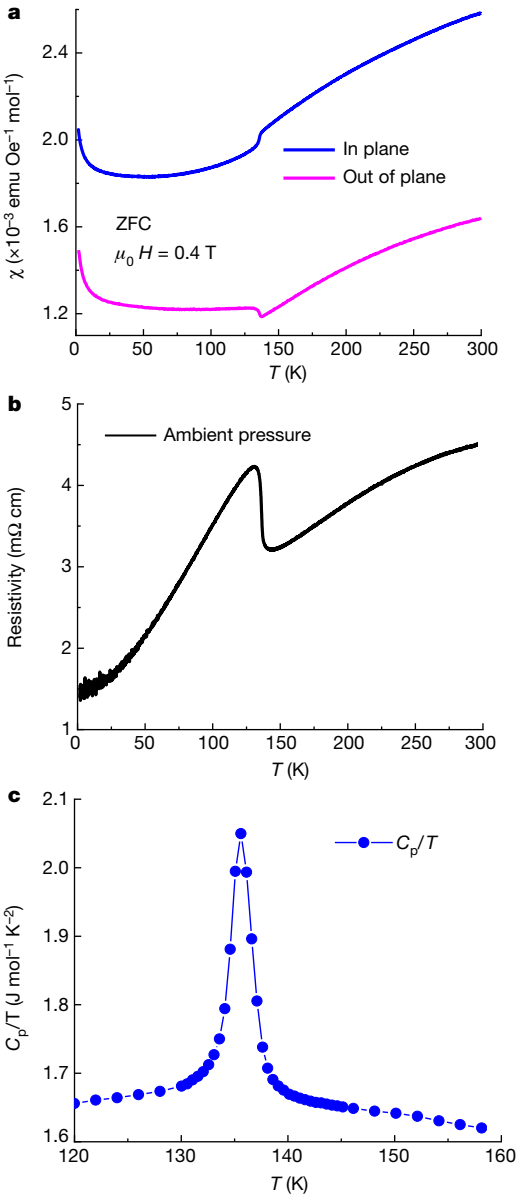

Fig. 2 | Magnetic susceptibility, resistivity and specific heat of $La_4Ni_3O_{10-\delta}$ single crystal at ambient pressure. a, Magnetic susceptibility of $La_4Ni_3O_{10-\delta}$ measured from 2 K to 300 K with an applied field of 0.4 T, parallel and perpendicular to the *ab* plane. The spin and charge order transition characterized by a kink in the $\chi(T)$ curve occurs at $T_N \approx 136$ K. **b**, Resistivity profile of $La_4Ni_3O_{10-\delta}$ in the *ab* plane at ambient pressure, using a current of 100 μA. **c**, Specific heat of $La_4Ni_3O_{10-\delta}$ near T_N.

$T_N \approx 136$ K (Fig. 2a), suggesting the emergence of the static spin–charge order, as previously shown in neutron diffraction experiments[36]. This phase transition was corroborated by heat capacity measurements, which exhibited a pronounced peak at a similar temperature (Fig. 2c). These results are consistent with the monoclinic $P2_1/a$ structure of the material at ambient pressure[34,39].

The electrical resistance $R(T)$ of $La_4Ni_3O_{10-\delta}$ single crystals under various pressure conditions is presented in Fig. 2b and Fig. 3a–e. At ambient pressure, $La_4Ni_3O_{10-\delta}$ exhibits a characteristic metallic behaviour, with resistivity exhibiting a decrease as the temperature descends below 300 K. A distinctive, steplike kink in the resistivity curve manifests at the spin–charge ordering temperature T_N (Fig. 2b). The spin and charge order phase transition observed in our measurements shows a marked sharpness, which is notable in comparison with previous studies. This indicates the high quality of our $La_4Ni_3O_{10-\delta}$

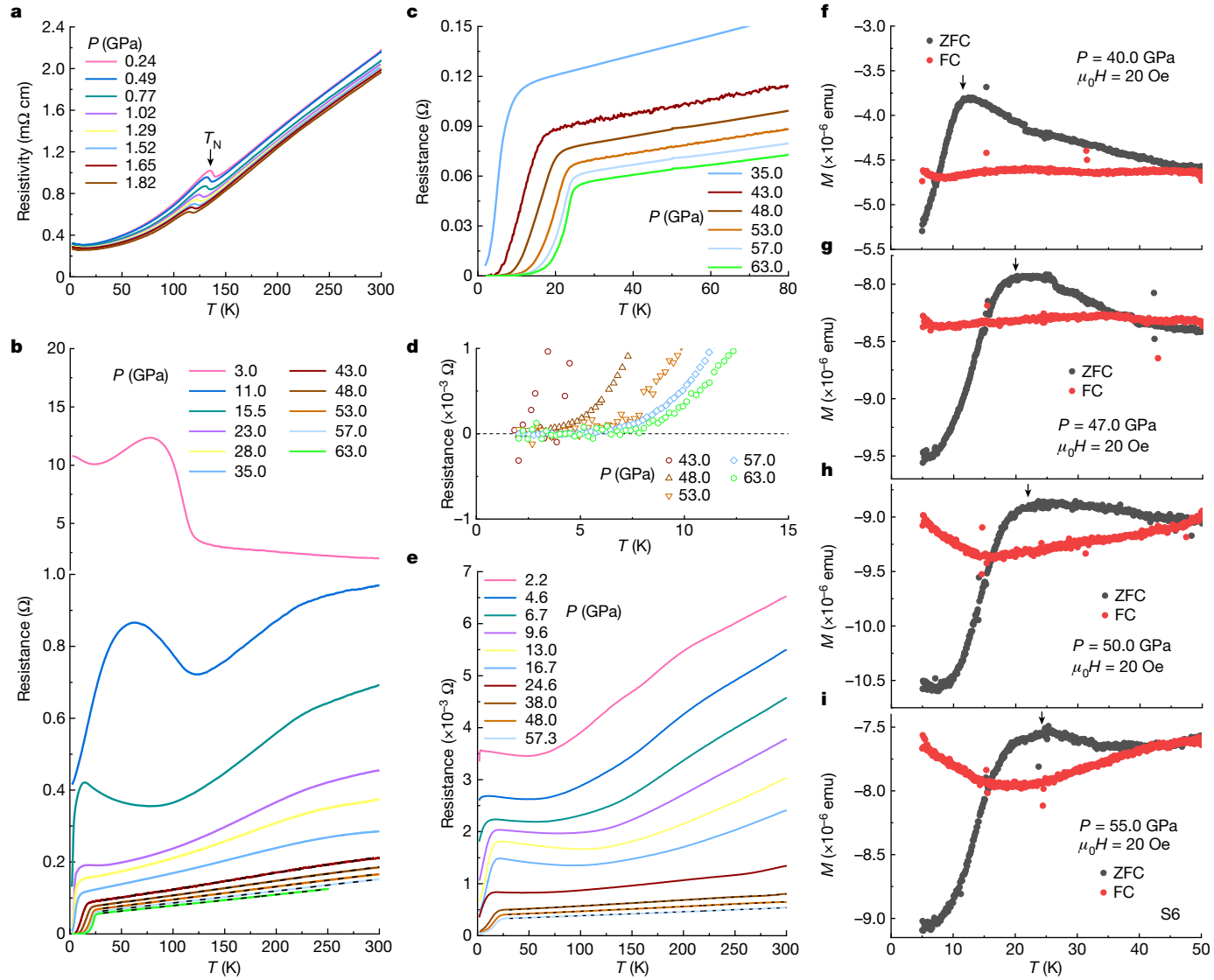

Fig. 3 | Temperature-dependent resistances and d.c. susceptibilities of $La_4Ni_3O_{10-\delta}$ single crystals under various pressures. a, Resistivity at pressures spanning 0.24 GPa to 1.82 GPa in the piston-cylinder cell, using a current of 2 mA. The spin and charge order transition at T_N is progressively suppressed with increasing pressure. **b**, Resistances at pressures ranging from 3.0 GPa to 63.0 GPa in the helium DAC for sample S3, using a current of 500 μA. The diamond broke on warming to around 250 K at 63.0 GPa. The black dashed lines depict the linear fit of the normal state resistances. **c**, Resistances in the helium DAC near the superconducting transition for S3. Zero resistances are observed above 43.0 GPa. **d**, An enlarged view of the resistance curve below T_c within the helium DAC, providing a demonstration of zero resistance for S3. **e**, Resistances at pressures ranging from 2.2 GPa to 57.3 GPa in the KBr DAC for sample S1, using a current of 100 μA. The black dashed lines depict the linear fit of the normal state resistances. **f**, Temperature-dependent magnetization curves of $La_4Ni_3O_{10-\delta}$ under a magnetic field of 20 Oe applied perpendicular to the *ab* plane using the ZFC and FC modes at 40.0 GPa for sample S6. **g**–**i**, A distinct superconducting diamagnetic response at T_c is observed in the ZFC curve for 47.0 GPa (**g**), 50.0 GPa (**h**) and 55.0 GPa (**i**). The black arrows indicate the superconducting transition temperatures.

single crystals, setting the stage for precise investigations into its physical properties under pressure.

When external pressure is exerted on the piston-cylinder cell, the characteristic kink related to the spin–charge ordering in the resistivity curve is rapidly suppressed (Fig. 3a), which is consistent with previous measurements on a powder sample below 1.28 GPa (ref. 40).

Resistances above 2.5 GPa were measured in a Be–Cu alloy diamond anvil cell (DAC). To ensure the best hydrostatic condition inside the DAC, we use helium as the pressure-transmitting medium. The resistance initially exhibits weak insulating behaviour, accompanied by a peak anomaly associated with the spin order transition at 3.0 GPa (Fig. 3b). As pressure increases, metallic behaviour is restored and the peak anomaly is progressively suppressed and, eventually, a sharp drop in resistance below a critical temperature T_c of 4.5 K is observed at 15.5 GPa (Fig. 3b). With further increments in pressure, T_c continues to rise, ultimately reaching a point at which zero resistance is observed at pressures exceeding 43.0 GPa (Fig. 3b–d). This signifies the emergence of superconductivity, with the onset superconducting transition temperature ranging from 4.5 K to around 30 K.

We also conducted temperature-dependent resistance measurements in a DAC using KBr as the pressure-transmitting medium. Across the pressure range spanning from 2.2 GPa to 24.6 GPa, a moderate decrease of resistance below a critical temperature of 2–20 K is observed (Fig. 3e). This together with the weak upturn in resistance in the normal state, indicates a limited superconducting volume, probably because of the filamentary nature of the superconductivity in this pressure range. As the pressure is raised further, a notable sharp reduction in resistance becomes evident at approximately 20–30 K, observed at pressures of 38.0 GPa and beyond (Fig. 3e) and the onset T_c reaches 30.1 K at 69.0 GPa (Fig. 3e and Extended Data Fig. 5). However,

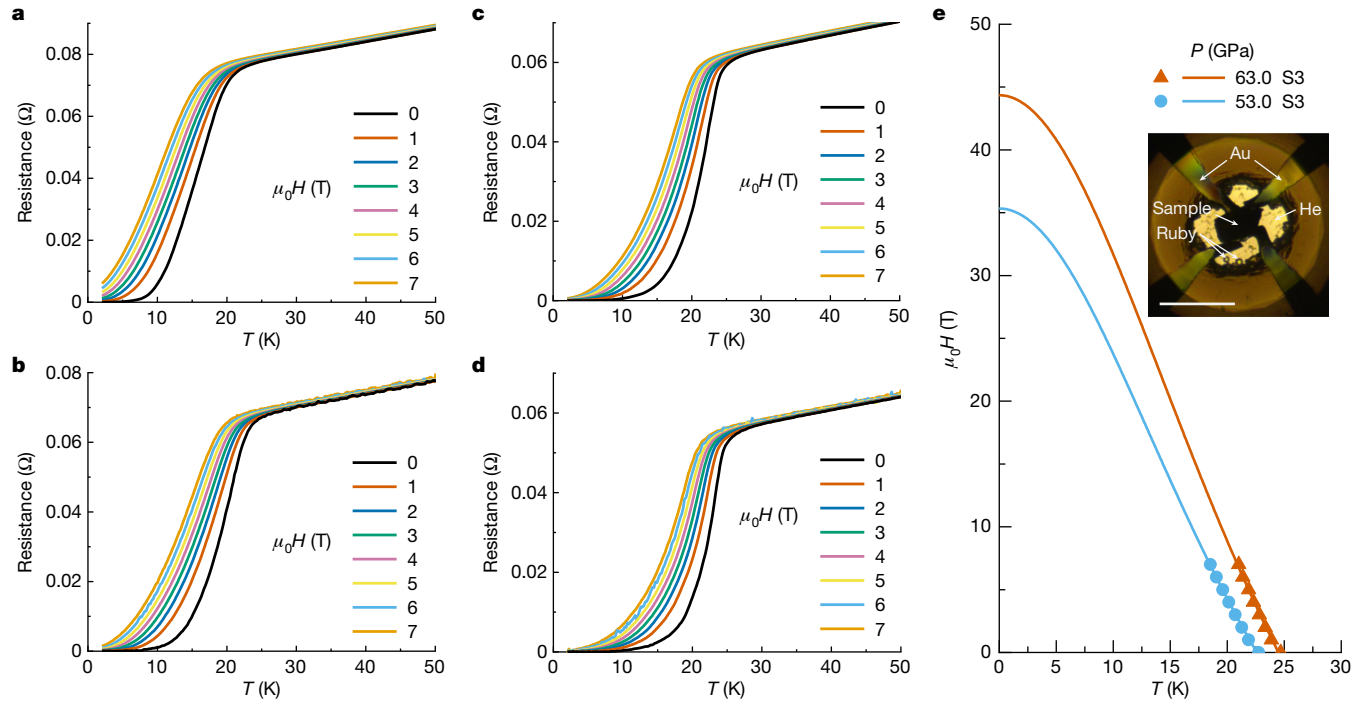

Fig. 4 | Magnetic field effects on the superconducting transition in $La_4Ni_3O_{10-\delta}$. **a**–**d**, Field dependences of electrical resistance for sample S3 at 48.0 GPa (**a**), 53.0 GPa (**b**), 57.0 GPa (**c**) and 63.0 GPa (**d**). **e**, The Ginzburg–Landau fittings of the upper critical fields at 53.0 GPa and 63.0 GPa. The magnetic fields are applied perpendicular to the *ab* plane. Inset, a photograph of the electrodes used for high-pressure resistance measurements. Scale bar, 100 μm (**e**, inset).

small residue resistance below T_c was observed in this configuration, probably attributed to the less hydrostatic conditions resulting from the pressure-transmitting medium KBr.

To provide further confirmation of the pressure-induced superconductivity, we conducted ultrasensitive d.c. magnetic susceptibility measurements under high pressures within a custom-built miniature Be–Cu alloy DAC, using nitrogen as the pressure-transmitting medium to provide a hydrostatic pressure environment. A distinctive diamagnetic response at T_c is evident in the zero-field-cooled (ZFC) curve at 40.0 GPa, and as pressure increases, T_c also rises, consistent with the resistance measurements, further confirming the emergence of superconductivity (Fig. 3f–i and Extended Data Fig. 8). We have estimated the maximum superconducting volume fraction to be around 86% across the pressures applied, suggesting the development of bulk superconductivity (Extended Data Fig. 9). Conversely, below 30 GPa, no prominent superconducting diamagnetic responses were detected, suggesting that the superconducting volume fraction is relatively limited at low pressures (Extended Data Fig. 10). The difference of susceptibilities between ZFC and field-cooled (FC) curves in the normal states is because of the magnetic background of the pressure cell with residual magnetic impurities (Supplementary Fig. 5).

Concomitant with the emergence of zero resistance at 43.0 GPa, the normal state resistance follows a linear temperature dependence up to 300 K (Fig. 3b). This behaviour is a hallmark of the so-called strange metal state, a characteristic phenomenon observed in optimal doped cuprates, certain iron-based materials and nickelate superconductors[2,17,18,41–45], implying the existence of strong correlations and underscores the unconventional nature of superconductivity. Similar strange metal behaviour was also confirmed in the measurements conducted within the KBr DAC above 38.0 GPa (Fig. 3e).

Figure 4a–d shows the temperature-dependent magnetoresistance measured in magnetic fields perpendicular to the *ab* plane under various pressures. As the magnetic field is increased, superconductivity is progressively suppressed, providing further confirmation that the transition in resistance is because of the onset of superconductivity. We use the 90% resistance transition to the normal state near T_c and fit it to the Ginzburg–Landau form $H_{c2}(T) = H_{c2}(0)[(1-t^2)/(1+t^2)]$, where $t = T/T_c$. This analysis yields an estimation of the upper critical field, with values reaching 44 T at 63.0 GPa when using the helium DAC, and 48 T at 69.0 GPa with the KBr DAC (Fig. 4e and Extended Data Fig. 5). These values of upper critical field exceed those observed in infinite-layer nickelates[13] but fall below $La_3Ni_2O_7$ (ref. 17).

Figure 1a summarizes the pressure-dependent spin–charge order and superconductivity phase diagram in trilayer $La_4Ni_3O_{10-\delta}$. This phase diagram bears some analogy to those found in cuprate and iron-based superconductors[2,21], in which high-T_c superconductivity arises on suppression of a static magnetic order. From the electronic structure perspective, it suggests that the d_{z^2} band could play an important part in shaping the pressure-dependent phase diagram of $La_4Ni_3O_{10-\delta}$. The d_{z^2} band is notably flat and shows a 20-meV spin-density wave-like gap[35]. This unique electronic structure feature, coupled with its propensity to interact with the *p*-orbital of apical oxygen, renders the d_{z^2} band highly susceptible to external pressure, with the potential to alter nesting conditions and influence the spin-density wave (SDW)–charge-density wave (CDW) order.

Therefore, the concurrent emergence of bulk superconductivity and strange metal behaviour could be attributed to the pressure effect that suppresses the density wave gap, brings the flat d_{z^2} band into proximity with the Fermi surface and consequently induces strong correlations and fosters the emergence of the strange metal behaviour. Simultaneously, the closing of the density wave gap dampens the static spin order and promotes dynamic spin fluctuations, paving the way for superconductivity to emerge, in which the hole Fermi surface associated with the $d_{x^2-y^2}$ orbital may also come into play.

If this analysis were extended to the bilayer system, it suggests that the absence of (or weak) static magnetic order in $La_3Ni_2O_7$ may be attributed to the fact that the d_{z^2} band lies considerably further below the Fermi level compared with $La_4Ni_3O_{10}$ (refs. 35,46). However, even the flat bands located away from the Fermi level have the potential to generate high-energy spin fluctuations, which could exert a noteworthy

influence on the phase diagram or serve as a mediator of electron pairing[47]. Further investigations in this direction are warranted to fully explain the role of magnetism in nickelate superconductors.

Furthermore, it is important to consider the impact of the interlayer coupling, a factor that could potentially promote superconductivity and has been intensively discussed in multilayer cuprates and bilayer $La_3Ni_2O_7$ (refs. 2,17,29,30,48). The observation of pressure-induced superconductivity accompanied by a structural transition from monoclinic to tetragonal phases also suggests a potential role of interlayer coupling in trilayer $La_4Ni_3O_{10-\delta}$. However, unlike cuprate superconductors for which the highest T_c is achieved in trilayer systems, in the case of trilayer $La_4Ni_3O_{10-\delta}$, the T_c is lower than that of bilayer $La_3Ni_2O_7$. This discrepancy suggests the presence of distinct interlayer interaction mechanisms between these two systems. Further investigations are needed to explain these coupling mechanisms, particularly focusing on differences in carrier concentrations and magnetic structures between the inner and outer NiO_2 layers, as well as the interlayer coupling between the two outer NiO_2 layers. These factors are crucial for understanding the evolution of T_c in multilayer superconductors[2,29,30,48].

In summary, we present evidence of bulk superconductivity in trilayer nickelate $La_4Ni_3O_{10-\delta}$ single crystals under pressure. Our experiments also show strange metal behaviour in the normal state, characterized by the linear temperature dependence of resistance up to 300 K, which may be linked to the enhanced spin fluctuations and strong correlations induced by the flat d_{z^2} band positioned near the Fermi level. Furthermore, the layer-dependent T_c in nickelates is distinct from that observed in cuprates, suggesting unique interlayer coupling and charge transfer mechanisms specific to nickelates. Further research is required to fully understand the precise role of interlayer coupling in the pairing, especially considering the differences in carrier concentrations and magnetism between the inner and outer NiO_2 layers, as well as the interlayer coupling between the two outer NiO_2 layers, which are absent in the bilayer system. Furthermore, a comprehensive exploration of the role of the $d_{x^2-y^2}$ orbital and pairing symmetry is necessary for a complete understanding. In essence, our findings establish a promising new material platform, inviting deeper exploration into the intricate interplay between spin–charge order, flat band structure, interlayer coupling, strange metal behaviour and high-T_c superconductivity. This avenue of research holds great potential for uncovering new phenomena and advancing our understanding of high-T_c superconductors.

Online content

Any methods, additional references, Nature Portfolio reporting summaries, source data, extended data, supplementary information, acknowledgements, peer review information; details of author contributions and competing interests; and statements of data and code availability are available at https://doi.org/10.1038/s41586-024-07553-3.

1. Bednorz, J. G. & Müller, K. A. Possible high T_c superconductivity in the Ba–La–Cu–O system. *Z. Phys. B Condens. Matter* **64**, 189–193 (1986).
2. Lee, P. A., Nagaosa, N. & Wen, X. G. Doping a Mott insulator: physics of high-temperature superconductivity. *Rev. Mod. Phys.* **78**, 17–85 (2006).
3. Scalapino, D. J. A common thread: the pairing interaction for unconventional superconductors. *Rev. Mod. Phys.* **84**, 1383–1417 (2012).
4. Kamihara, Y., Watanabe, T., Hirano, M. & Hosono, H. Iron-based layered superconductor La[$O_{1-x}F_x$]FeAs (x = 0.05–0.12) with T_c = 26 K. *J. Am. Chem. Soc.* **130**, 3296–3297 (2008).
5. Maeno, Y. et al. Superconductivity in a layered perovskite without copper. *Nature* **372**, 532–534 (1994).
6. Wang, F. & Senthil, T. Twisted Hubbard model for Sr_2IrO_4: magnetism and possible high temperature superconductivity. *Phys. Rev. Lett.* **106**, 136402 (2011).
7. Kim, Y. K., Sung, N. H., Denlinger, J. D. & Kim, B. J. Observation of a *d*-wave gap in electron-doped Sr_2IrO_4. *Nat. Phys.* **12**, 37–41 (2016).
8. Anisimov, V. I., Bukhvalov, D. & Rice, T. M. Electronic structure of possible nickelate analogs to the cuprates. *Phys. Rev. B* **59**, 7901–7906 (1999).
9. Lee, K.-W. & Pickett, W. E. Infnite-layer $LaNiO_2$: Ni^{1+} is not Cu^{2+}. *Phys. Rev. B* **70**, 165109 (2004).
10. Chaloupka, J. & Khaliullin, G. Orbital order and possible superconductivity in $LaNiO_3/LaMO_3$ superlattices. *Phys. Rev. Lett.* **100**, 016404 (2008).
11. Zhang, J. et al. Stacked charge stripes in the quasi-2D trilayer nickelate $La_4Ni_3O_8$. *Proc. Natl Acad. Sci. USA* **113**, 8945–8950 (2016).
12. Lechermann, F. Late transition metal oxides with infinite-layer structure: nickelates versus cuprates. *Phys. Rev. B* **101**, 081110 (2020).
13. Li, D. et al. Superconductivity in an infinite-layer nickelate. *Nature* **572**, 624–627 (2019).
14. Zeng, S. et al. Phase diagram and superconducting dome of infinite-layer $Nd_{1-x}Sr_xNiO_2$ thin films. *Phys. Rev. Lett.* **125**, 147003 (2020).
15. Pan, G. A. et al. Superconductivity in a quintuple-layer square-planar nickelate. *Nat. Mater.* **21**, 160–164 (2022).
16. Ding, X. et al. Critical role of hydrogen for superconductivity in nickelates. *Nature* **615**, 50–55 (2023).
17. Sun, H. et al. Signatures of superconductivity near 80 K in a nickelate under high pressure. *Nature* **621**, 493–498 (2023).
18. Zhang, Y. et al. High-temperature superconductivity with zero-resistance and strange metal behavior in $La_3Ni_2O_{7-\delta}$. Preprint at arxiv.org/abs/2307.14819 (2023).
19. Zhou, Y. et al. Evidence of filamentary superconductivity in pressurized $La_3Ni_2O_7$. Preprint at arxiv.org/abs/2311.12361 (2023).
20. Wang, G. et al. Pressure-induced superconductivity in polycrystalline $La_3Ni_2O_{7-\delta}$. *Phys. Rev. X* **14**, 011040 (2024).
21. Dai, P. Antiferromagnetic order and spin dynamics in iron-based superconductors. *Rev. Mod. Phys.* **87**, 855–896 (2015).
22. Ling, C. D. et al. Neutron diffraction study of $La_3Ni_2O_7$: structural relationships among n = 1, 2, and 3 phases $La_{n+1}Ni_nO_{3n+1}$. *J. Solid State Chem.* **152**, 517–525 (1999).
23. Gu, Y. et al. Effective model and pairing tendency in bilayer Ni-based superconductor $La_3Ni_2O_7$. Preprint at arxiv.org/abs/2306.07275 (2023).
24. Scott, B. A. et al. Layer dependence of the superconducting transition temperature of $HgBa_2Ca_{n-1}Cu_nO_{2n+2+\delta}$. *Physica C* **230**, 239–245 (1994).
25. Kuzemskaya, I. G., Kuzemsky, A. L. & Cheglokov, A. A. Superconducting properties of the family of mercurocuprates and role of layered structure. *J. Low-Temp. Phys.* **118**, 147–152 (2000).
26. Iyo, A. et al. T_c vs n relationship for multilayered high-T_c superconductors. *J. Phys. Soc. Jpn.* **76**, 094711 (2007).
27. Schilling, A., Cantoni, M., Guo, J. D. & Ott, H. R. Superconductivity above 130 K in the Hg–Ba–Ca–Cu–O system. *Nature* **363**, 56–58 (1993).
28. Gao, L. et al. Superconductivity up to 164 K in $HgBa_2Ca_{m-1}Cu_mO_{2m+2+\delta}$ (m = 1, 2, and 3) under quasihydrostatic pressures. *Phys. Rev. B* **50**, 4260–4263 (1994).
29. Chakravarty, S., Kee, H.-Y. & Völker, K. An explanation for a universality of transition temperatures in families of copper oxide superconductors. *Nature* **428**, 53–55 (2004).
30. Berg, E., Orgad, D., Kivelson, & Steven, A. Route to high-temperature superconductivity in composite systems. *Phys. Rev. B* **78**, 094509 (2008).
31. Botana, A. S., Pardo, V. & Norman, M. R. Electron doped layered nickelates: spanning the phase diagram of the cuprates. *Phys. Rev. Mater.* **1**, 021801 (2017).
32. Nica, E. M. et al. Theoretical investigation of superconductivity in trilayer square-planar nickelates. *Phys. Rev. B* **102**, 020504 (2020).
33. Cheng, J.-G. et al. Pressure effect on the structural transition and suppression of the high-spin state in the triple-layer T'-$La_4Ni_3O_8$. *Phys. Rev. Lett.* **108**, 236403 (2012).
34. Zhang, J. et al. High oxygen pressure floating zone growth and crystal structure of the metallic nickelates $R_4Ni_3O_{10}$ (R = La, Pr). *Phys. Rev. Mater.* **4**, 083402 (2020).
35. Li, H. et al. Fermiology and electron dynamics of trilayer nickelate $La_4Ni_3O_{10}$. *Nat. Commun.* **8**, 704 (2017).
36. Zhang, J. et al. Intertwined density waves in a metallic nickelate. *Nat. Commun.* **11**, 6003 (2020).
37. Hu, W. Z. et al. Origin of the spin density wave instability in AFe_2As_2 (A = Ba, Sr) as revealed by optical spectroscopy. *Phys. Rev. Lett.* **101**, 257005 (2008).
38. Li, J. et al. Structural transition, electric transport, and electronic structures in the compressed trilayer nickelate $La_4Ni_3O_{10}$. *Sci. China-Phys. Mech. Astron.* **67**, 117403 (2024).
39. Yuan, N. et al. High-pressure crystal growth and investigation of the metal-to-metal transition of Ruddlesden–Popper trilayer nickelates $La_4Ni_3O_{10}$. *J. Cryst. Growth* **627**, 127511 (2024).
40. Wu, G., Neumeier, J. J. & Hundley, M. F. Magnetic susceptibility, heat capacity, and pressure dependence of the electrical resistivity of $La_3Ni_2O_7$ and $La_4Ni_3O_{10}$. *Phys. Rev. B* **63**, 245120 (2001).
41. Gurvitch, M. & Fiory, A. T. Resistivity of $La_{1.825}Sr_{0.175}CuO_4$ and $YBa_2Cu_3O_7$ to 1100 K: absence of saturation and its implications. *Phys. Rev. Lett.* **59**, 1337–1340 (1987).
42. Kasahara, S. et al. Evolution from non-Fermi- to Fermi-liquid transport via isovalent doping in $BaFe_2(As_{1-x}P_x)_2$ superconductors. *Phys. Rev. B* **81**, 184519 (2010).
43. Yuan, J. et al. Scaling of the strange-metal scattering in unconventional superconductors. *Nature* **602**, 431–436 (2022).
44. Jiang, X. et al. Interplay between superconductivity and the strange-metal state in FeSe. *Nat. Phys.* **19**, 365–371 (2023).
45. Lee, K. et al. Linear-in-temperature resistivity for optimally superconducting (Nd,Sr)NiO_2. *Nature* **619**, 288–292 (2023).
46. Yang, J. et al. Orbital-dependent electron correlation in double-layer nickelate $La_3Ni_2O_7$. Preprint at arxiv.org/abs/2309.01148 (2023).
47. Wang, F. et al. The electron pairing of $K_xFe_{2-y}Se_2$. *Europhys. Lett.* **93**, 57003 (2011).
48. Luo, X. et al. Electronic origin of high superconducting critical temperature in trilayer cuprates. *Nat. Phys.* **19**, 1841–1847 (2023).

Methods

Growth of $La_4Ni_3O_{10-\delta}$ single crystals

The precursor powder for the $La_4Ni_3O_{10-\delta}$ compound was prepared using the conventional solid-state reaction method. Chemically stoichiometric raw materials, La_2O_3 and NiO (Aladdin, 99.99%), were meticulously ground and mixed using a Vibratory Micro Mill (FRITSCH PULVERISETTE 0). An additional 0.5% of NiO was included to compensate for potential NiO volatilization during the crystal growth process. The resulting mixture underwent calcination at 1,373 K for 24 h, with two repeated calcination cycles to ensure complete and homogeneous reactions.

Subsequently, the resulting precursor material was pressed into a cylindrical rod, approximately 13 cm in length and 6 mm in diameter, using a hydrostatic pressure of 300 MPa. The shaped rod then underwent once sintering at 1,673 K for 12 h in air. Single crystals were grown using a vertical optical-image floating-zone furnace (Model HKZ, SciDre) at Fudan University. During the crystal growth process, we carefully maintained an oxygen pressure of 18–22 bar, and used a 5-kW Xenon arc lamp as the light source. The rod was rapidly traversed through the growth zone at a speed of 15 mm h^{-1} to enhance the density, after which a growth rate of 3 mm h^{-1} was maintained.

STEM measurements

The scanning transmission electron microscopy (STEM) experiments were performed on a double aberration-corrected S/TEM (Themis Z, Thermo Fisher Scientific) operated at 300 kV. For STEM-HAADF imaging, the probe semi-convergent angle is 21.4 mrad, and the HAADF collection angle is from 79 mrad to 200 mrad. The atomic-resolution EDX imaging was recorded with a Super-X detector.

Measurements under high pressure

We conducted electrical resistance measurements on $La_4Ni_3O_{10-\delta}$ single crystals under pressure in a physical property measurement system by Quantum Design. The temperature range covered was from 1.8 K to 300 K, and magnetic fields of up to 9 T were applied. The electrical resistivity measurements at low pressures (below 2.5 GPa) were performed in a piston-cylinder cell using the standard four-probe method (Fig. 3a). The pressure-transmitting medium used in this setup was liquid Daphne 7373. The pressure was calibrated from the superconducting transition temperature of Pb. The electrical resistance measurements at high pressures (above 2.2 GPa) were performed in a DAC with 200–300 μm culets using the standard van der Pauw four-probe method (Figs. 3b–d and 4 and Extended Data Fig. 4). The sample chamber was constructed using a mixture of cubic boron nitride and epoxy, with a diameter ranging from 140 μm to 280 μm. The single crystal was loaded under helium as the pressure-transmitting medium. KBr powders were also used as a different pressure-transmitting medium (Fig. 3e and Extended Data Fig. 5). Pressure calibration was carried out using ruby fluorescence peak shift at room temperature.

Ultrasensitive magnetic susceptibility measurements under pressure were conducted using a custom-built beryllium-copper alloy miniature DAC equipped with a rhenium gasket, using a design similar to that in refs. 49,50. The mini-DAC has dimensions of approximately 8.5 mm in diameter and 30 mm in length. The measurements were performed using a Magnetic Property Measurement System (MPMS3, Quantum Design). The DAC includes a pair of diamond anvils with a diameter of 300 μm and a sample chamber with a diameter of 210 μm. The sample chamber was filled with a single crystal of $La_4Ni_3O_{10-\delta}$ and liquid nitrogen as the pressure-transmitting medium to provide a hydrostatic pressure environment. The samples had a diameter of approximately 150–200 μm and a thickness of roughly 25 μm.

The single-crystal neutron-diffraction experiments were performed using the HB-3A four-circle single-crystal neutron diffractometer at the High Flux Isotope Reactor at Oak Ridge National Laboratory. An Si (220) monochromatic neutron beam with a wavelength of 1.533 Å was used for the measurements. In situ lab-based high-pressure XRD measurements on powder and single crystals were carried out using a Bruker D8 Venture diffractometer, using Mo Kα radiation (λ = 0.7107 Å) in a DAC with 300-μm-diameter culets and stainless steel gaskets (Extended Data Figs. 2 and 7, Supplementary Fig. 9 and Supplementary Tables 1 and 2). A methanol:ethanol:water mixture in the ratio of 16:3:1 was used as the pressure-transmitting medium for these measurements. For the powder measurements, we captured two-dimensional patterns of powder diffraction rings, which were subsequently processed to yield one-dimensional profiles (Extended Data Fig. 2). We included a small ruby ball within the chamber to facilitate pressure calibration by monitoring the fluorescence peak shift of ruby. In situ synchrotron-based high-pressure XRD measurements were performed at the beamline 15U1 at Shanghai Synchrotron Radiation Facility, using an X-ray beam with a wavelength of 0.6199 Å (Extended Data Figs. 1b and 3 and Supplementary Table 3). A symmetric DAC with anvil culet sizes of 300 μm and rhenium gaskets were used. Helium was used as the pressure-transmitting medium to maintain optimal hydrostatic pressure conditions, with pressure calibration again based on the shift in the fluorescence peak of a ruby indicator.

Calculation of superconducting volume fraction

The susceptibility χ_m of a superconductor can be decomposed into

$$\chi_m = (1-f)\chi_p + f\chi_d, \quad (1)$$

where f is the superconducting volume fraction, χ_p denotes the paramagnetic susceptibility and χ_d denotes the diamagnetic susceptibility.

In SI units, $\chi_d = -1$, and $\chi_p \to 0$, equation (1) can be then expressed as

$$f = |\chi_m|, \quad (2)$$

On converting between unit systems, the susceptibility equation becomes

$$\chi_{SI} = 4\pi\chi_{CGS} = 4\pi M/H = 4\pi \sum \mu_i / \sum V_i = (4\pi\mu m_a)/(HVN_a m), \quad (3)$$

where $\mu \approx 1.69 \times 10^{-6}$ emu represents the measured magnetic moment at 5 K after subtracting the constant background signal at the onset of T_c for sample S6 at 20 Oe and 50 GPa. $m \approx 3.16$ μg is the sample mass that was calculated based on the refined density ρ = 7.16 g cm^{-3} and the sample volume at ambient condition; m_a is the molar mass, N_a is the Avogadro constant and V = 342.837 $Å^3$ is the cell volume for an $I4/mmm$ primitive cell with Z = 2 at 50 GPa (Fig. 1d and Supplementary Table 3).

The demagnetizing factor N of a finite cylinder with an axial magnetic field can be approximated using[51]

$$N^{-1} \approx 1 + 1.6(C/A), \quad (4)$$

where A is the diameter and C is the thickness of the sample. For sample S6, A = 160 μm and C = 22 μm at ambient conditions, yielding a demagnetizing factor of N = 0.82. This factor remains largely unchanged under hydrostatic pressure because of the proportional contraction of the lattice dimensions of the crystal structure (Supplementary Table 3). The susceptibility χ can be calculated as

$$N = 1/\chi_0 - 1/\chi, \quad (5)$$

where χ_0 is the measured value and χ is the adjusted susceptibility for the sample geometry. Implementing the above procedure, χ calculates to approximately −0.86 at 5 K for S6, indicating a superconducting volume fraction of 86% as shown in Extended Data Fig. 9. This substantiates pressure-induced bulk superconductivity in $La_4Ni_3O_{10-\delta}$.

Extended analysis and discussion

The upper critical fields of nickelates are comparable with those observed in hole-doped cuprate and iron-pnictide superconductors exhibiting similar T_c values[52–54] but surpass those of simple conventional superconductors[49,55]. Furthermore, our estimation of the in-plane superconducting coherence length of $La_4Ni_3O_{10-\delta}$ approximates to 26 Å at 69.0 GPa, close to values of 122 iron pnictide and $La_{2-x}Sr_xCuO_4$ (refs. 52–54). The high upper critical fields and the correspondingly shorter superconducting coherence lengths point to tightly bound Cooper pairs, hinting at an unconventional pairing mechanism possibly driven by spin fluctuations and strong electronic correlations. Theoretical calculations on both infinite-layered and bilayer nickelates suggest that electron–phonon coupling alone is insufficient to account for the observed high critical temperatures[56,57]. We anticipate that the scenario for $La_4Ni_3O_{10}$ is similar, although specific calculations for this material have not yet been published in the literature.

Recently, several theoretical preprints on $La_4Ni_3O_{10}$ have appeared, examining its intricate electronic structure, the unique layer-dependent magnetism of its trilayer configuration and its superconductivity. These analyses underscore the impact of electronic correlations, spin fluctuations and interlayer coupling on the strange metal behaviour of the material and its unconventional superconducting pairing mechanism, with an emphasis on the $s_{\pm}$-wave pairing symmetry[58–64]. It has been suggested that the magnetic structures in $La_4Ni_3O_{10}$ vary substantially between the inner and outer NiO_2 layers, in which the inner layer is non-magnetic and the outer layers are antiferromagnetic[61–63]. There are also likely variations in carrier concentrations and electron correlations across these layers[58–64]. These distinctions in magnetic structure and electron dynamics potentially introduce a unique phenomenon not present in bilayer and infinite-layer nickelates, warranting further exploration.

While preparing this paper, we found three related studies that reported resistance measurements on $La_4Ni_3O_{10}$ polycrystalline samples[65–67]. In refs. 66,67, a reduction in resistance—ranging from 4% to 7% below the 15–20 K temperature range—under pressures exceeding roughly 30 GPa is observed, whereas in ref. 65 this phenomenon is not observed below 50 GPa.

Data availability

Source data are provided with this paper.

49. Drozdov, A. P., Eremets, M. I., Troyan, I. A., Ksenofontov, V. & Shylin, S. I. Conventional superconductivity at 203 kelvin at high pressures in the sulfur hydride system. *Nature* **525**, 73–76 (2015).
50. Deng, L. et al. Higher superconducting transition temperature by breaking the universal pressure relation. *Proc. Natl Acad. Sci. USA* **116**, 2004–2008 (2019).
51. Prozorov, R. & Kogan, V. G. Effective demagnetizing factors of diamagnetic samples of various shapes. *Phys. Rev. APP.* **10**, 014030 (2018).
52. Grissonnanche, G. et al. Direct measurement of the upper critical field in cuprate superconductors. *Nat. Commun.* **5**, 3280 (2014).
53. Ando, Y. et al. Resistive upper critical fields and irreversibility lines of optimally doped high-T_c cuprates. *Phys. Rev. B* **60**, 12475 (1999).
54. Johnston, D. C. The puzzle of high temperature superconductivity in layered iron pnictides and chalcogenides. *Adv. Phys.* **59**, 803–1061 (2010).
55. Thompson, J. D., Maley, M. P., Newkirk, L. R. & Bartlett, R. J. High-field properties and scaling in CVD-prepared Nb_3Ge. *J. Appl. Phys.* **50**, 977–982 (1979).
56. Meier, Q. N. et al. Preempted phonon-mediated superconductivity in the infinite-layer nickelates. *Phys. Rev. B* **109**, 184505 (2024).
57. Ouyang, Z., Gao, M. & Lu Z.-Y. Absence of phonon-mediated superconductivity in $La_3Ni_2O_7$ under pressure. Preprint at arxiv.org/abs/2403.14400 (2024).
58. Leonov, I. V. Electronic structure and magnetic correlations in trilayer nickelate superconductor $La_4Ni_3O_{10}$ under pressure. Preprint at arxiv.org/abs/2401.07350 (2024).
59. Tian, P., Ma, H.-T., Ming, X., Zheng, X.-J. & Li, H. Effective model and electron correlations in trilayer nickelate superconductor $La_4Ni_3O_{10}$. Preprint at arxiv.org/abs/2402.02351 (2024).
60. Wang, J., Ouyang, Z., He, R.-Q. & Lu, Z.-Y. Non-Fermi liquid and Hund correlation in $La_4Ni_3O_{10}$ under high pressure. *Phys. Rev. B* **109**, 165140 (2024).
61. LaBollita, H., Kapeghian, J., Norman, M. R. & Botana, A. S. Electronic structure and magnetic tendencies of trilayer $La_4Ni_3O_{10}$ under pressure: Structural transition, molecular orbitals, and layer differentiation. *Phys. Rev. B* **109**, 195151 (2024).
62. Zhang, Y., Lin, L.-F., Moreo, A., Maier, T. A. & Dagotto, E. Prediction of $s^{\pm}$-wave superconductivity enhanced by electronic doping in trilayer nickelates $La_4Ni_3O_{10}$ under pressure. Preprint at arxiv.org/abs/2402.05285 (2024).
63. Yang, Q.-G., Jiang, K.-Y., Wang, D., Lu, H.-Y. & Wang, Q.-H. Effective model and $s_{\pm}$-wave superconductivity in trilayer nickelate $La_4Ni_3O_{10}$. Preprint at arxiv.org/html/2402.05447v2 (2024).
64. Lu, C., Pan, Z., Yang, F. & Wu, C. Superconductivity in $La_4Ni_3O_{10}$ under pressure. Preprint at arxiv.org/abs/2402.06450 (2024).
65. Zhang, M. et al. Effects of pressure and doping on Ruddlesden-Popper phases $La_{n+1}Ni_nO_{3n+1}$. *J. Mater. Sci. Technol.* **185**, 147–154 (2024).
66. Sakakibara, H. et al. Theoretical analysis on the possibility of superconductivity in the trilayer Ruddlesden-Popper nickelate $La_4Ni_3O_{10}$ under pressure and its experimental examination: comparison with $La_3Ni_2O_7$. *Phys. Rev. B* **109**, 144511 (2024).
67. Li, Q. et al. Signature of superconductivity in pressurized $La_4Ni_3O_{10}$. *Chinese Phys. Lett.* **41**, 017401 (2024).

Acknowledgements This work was supported by the Key Program of the National Natural Science Foundation of China (grant no. 12234006), the National Key R&D Program of China (grant no. 2022YFA1403202), the Innovation Program for Quantum Science and Technology (grant no. 2024ZD0300103), the Beijing Natural Science Foundation (grant no. Z200005) and the Shanghai Municipal Science and Technology Major Project (grant no. 2019SHZDZX01). Y.Z. was supported by the Youth Foundation of the National Natural Science Foundation of China (grant no. 12304173). H.W. was supported by the Youth Foundation of the National Natural Science Foundation of China (grant no. 12204108). B.P. was supported by the Natural Science Foundation of Shandong Province (grant no. ZR2020YQ03). D.P. and Q.Z. acknowledge the financial support from the Shanghai Science and Technology Committee (no. 22JC1410300) and Shanghai Key Laboratory of Material Frontiers Research in Extreme Environments (no. 22dz2260800). A portion of this work was carried out at the Synergetic Extreme Condition User Facility (SECUF). A portion of this research used resources at the High Flux Isotope Reactor, a DOE Office of Science User Facility operated by the Oak Ridge National Laboratory. A portion of this research used resources at the beamline 15U1 of Shanghai synchrotron radiation facility.

Author contributions J.Z. planned the project; Y.Z., E.Z. and L.C. synthesized the single-crystal samples; Y.Z., F. Liu, E.Z., L.C., H.W., Yiqing Gu and Yimeng Gu performed the thermodynamic and transport measurements at ambient conditions; E.Z., B.P., Xu Chen, D.P., W.W. and J.W. performed the resistance measurements under pressure with the support of J.G., Q.Z., L.J. and J.Z.; H.R., T.Y., Xiaolong Chen and Y.S. assisted the resistance measurement under pressure. D.P. and Z.X. conducted the susceptibility measurements under pressure with the support of Q.Z.; N.L., Y.Z., D.P. and F. Lan performed the synchrotron XRD measurements and analysis with the support of W.Y. and Q.Z.; J.H. and Y.Z. conducted the S/TEM characterization with the support of C.Z.; D.J., Y.Z. and Y.H. performed the in-house powder and single-crystal diffraction measurements under pressure and data analysis with the support of H.G., H.C. and J.Z.; Y.H. performed the neutron single-crystal diffraction measurements and data analysis; J.Z., Y.Z. and F. Liu analysed the data; and J.Z., B.P. and Y.Z. wrote the paper. All authors provided comments on the paper.

Competing interests The authors declare no competing interests.

Additional information

Supplementary information The online version contains supplementary material available at https://doi.org/10.1038/s41586-024-07553-3.

Correspondence and requests for materials should be addressed to Qiaoshi Zeng, Jian-gang Guo or Jun Zhao.

Peer review information *Nature* thanks Pierre Toulemonde, Weiwei Xie and the other, anonymous, reviewer(s) for their contribution to the peer review of this work.

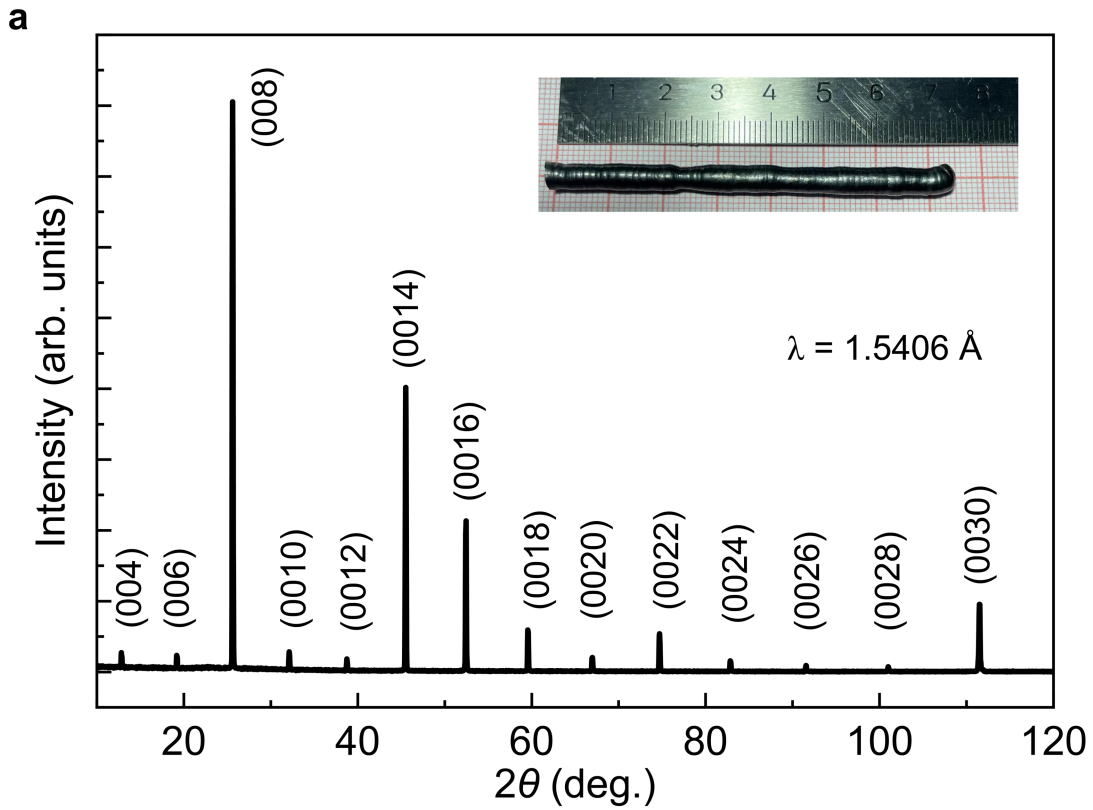

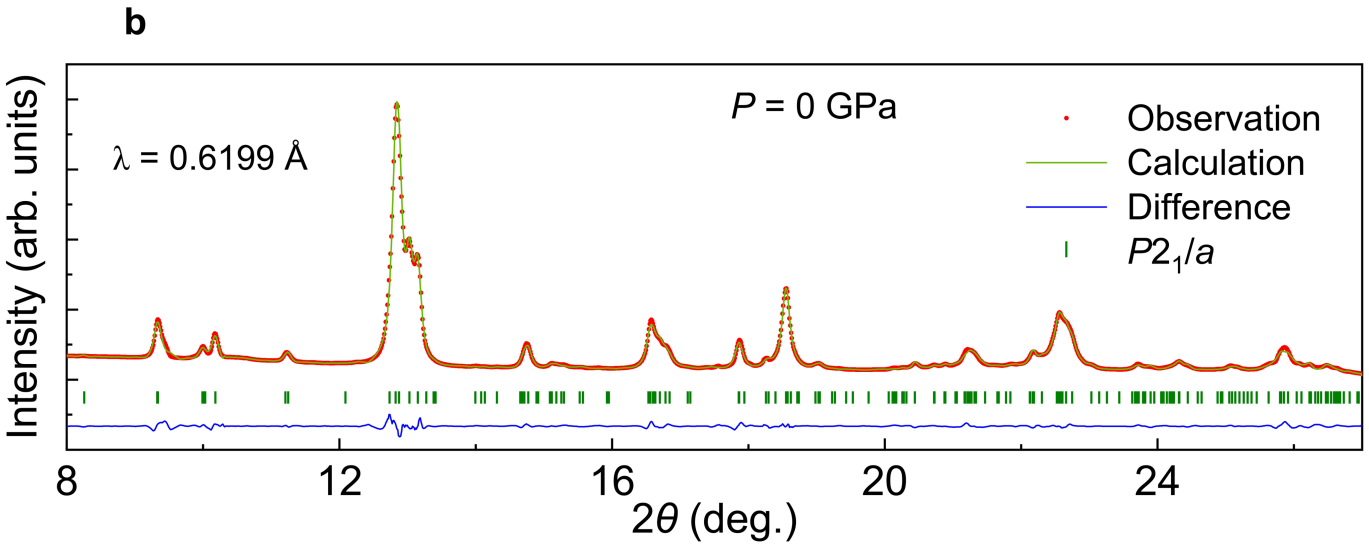

Extended Data Fig. 1 | XRD measurements of $La_4Ni_3O_{10-\delta}$ single crystals and powdered single crystals. a, XRD measurements of a $La_4Ni_3O_{10-\delta}$ single crystal along the *ab* plane, revealing no detectable impurity phases. The measurements were carried out on a Bruker D8 Discover diffractometer, utilizing Cu Kα radiation. The inset displays a photograph of a $La_4Ni_3O_{10-\delta}$ single crystal, grown using the high-pressure floating-zone method. **b**, Rietveld refinement of synchrotron-based powder XRD pattern of $La_4Ni_3O_{10-\delta}$ at ambient pressure and room temperature. The olive solid lines and red circles represent the fitted and experimental data, respectively. The blue solid lines indicate the intensity difference between the data and calculations. The short vertical bars indicate the Bragg peak positions. The data can be well described with the space group $P2_1/a$. The data were collected using a powdered $La_4Ni_3O_{10-\delta}$ single crystal. The refinement parameters are summarized in Supplementary Table 3.

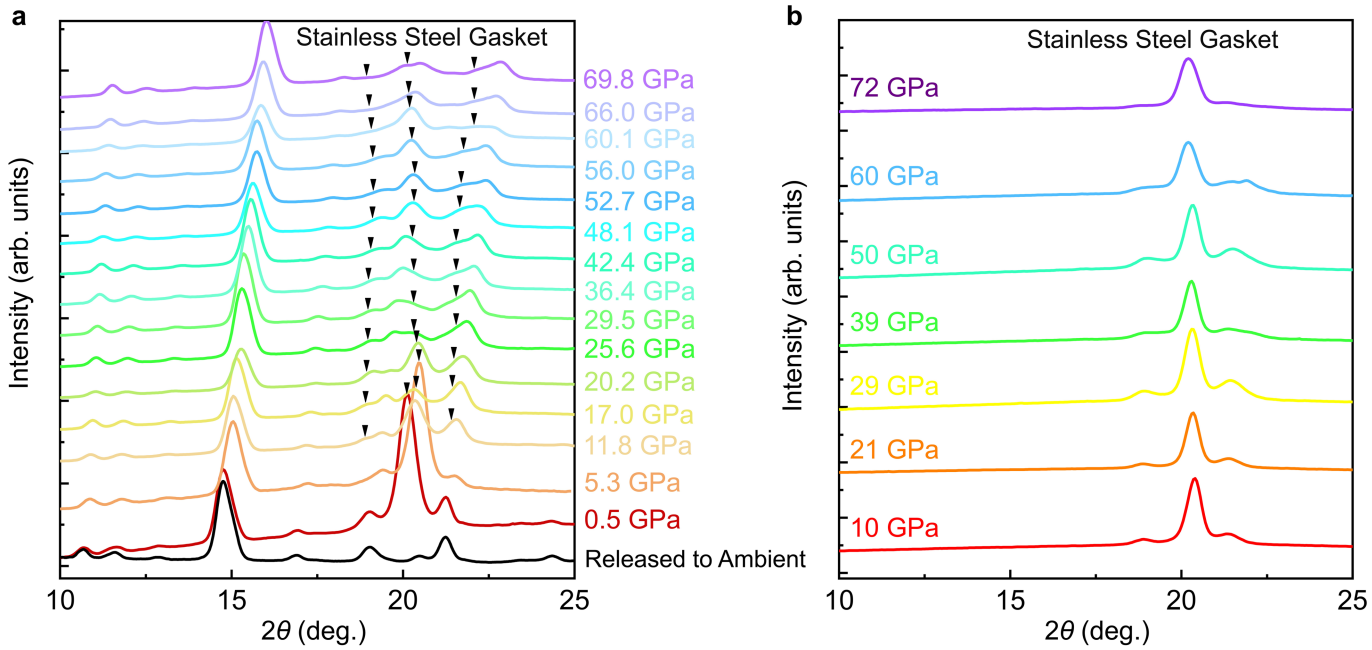

Extended Data Fig. 2 | Lab-based XRD measurements of a powdered $La_4Ni_3O_{10-\delta}$ single crystal at various pressures at room temperature. a, XRD measurements at various indicated pressures. The black arrows indicate the intensities from stainless steel. Upon releasing pressure to ambient condition, the diffraction pattern (black solid line) remains essentially unaltered in comparison to the data obtained prior to applying pressure, indicating that the process is reversible and the sample is stable against pressure. The structural transition observed in synchrotron-based XRD was not resolved in this measurement due to limited resolution. **b**, Measurements of empty cell with stainless steel gasket at indicated pressures at room temperature.

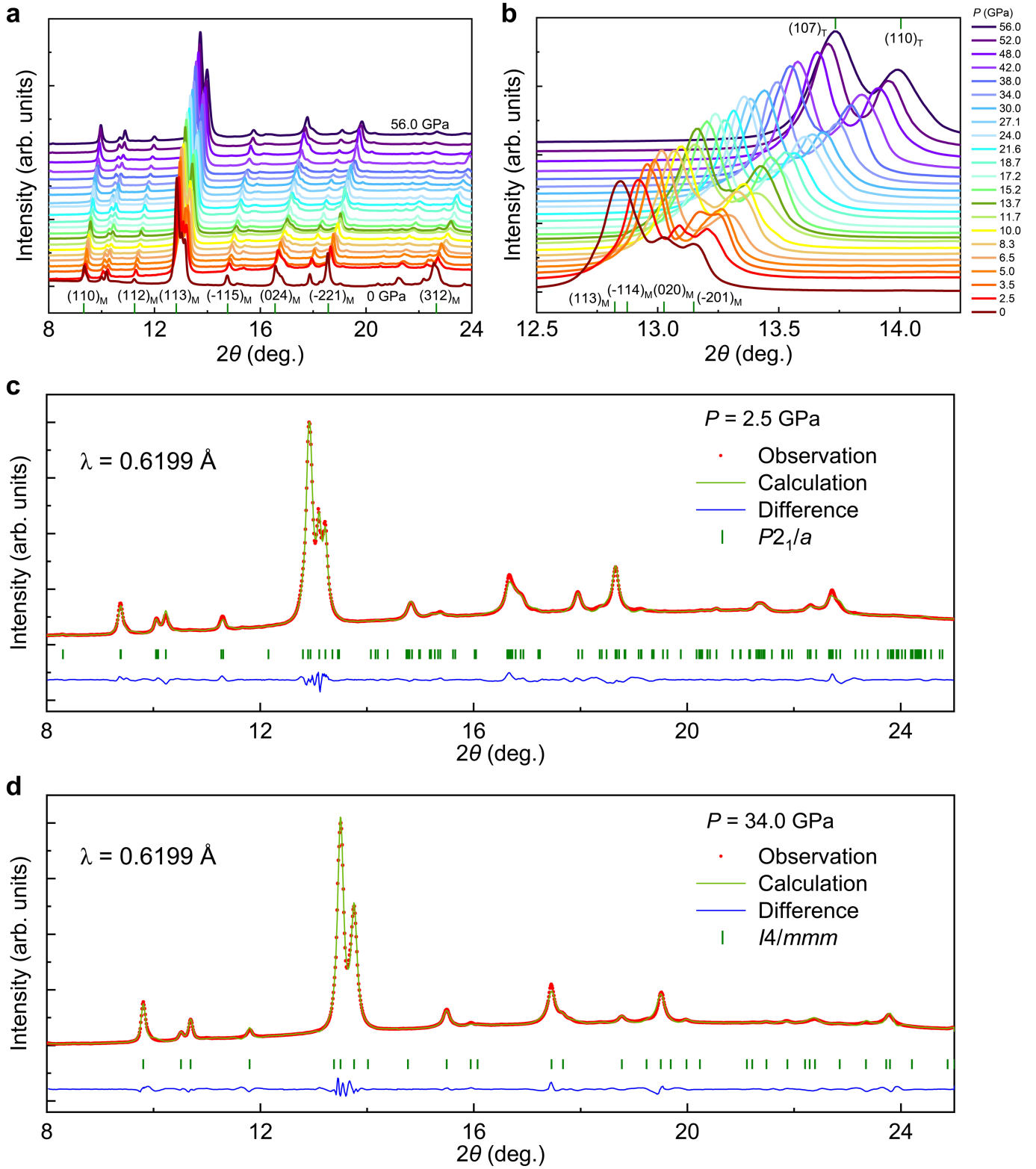

Extended Data Fig. 3 | Synchrotron-based XRD measurements of powdered $La_4Ni_3O_{10-\delta}$ single crystals under various pressures, using a helium DAC at room temperature. a, XRD measurements under various pressures. **b**, An enlarge view of diffraction peaks within the range of $12.5° < 2\theta < 14°$, illustrating the merging of the monoclinic $(0\,2\,0)_M$ and $(-2\,0\,1)_M$ peaks into the tetragonal $(1\,1\,0)_T$ peak, a clear indication of the structural phase transition from monoclinic to tetragonal. **c**, Rietveld refinement of XRD pattern of $La_4Ni_3O_{10-\delta}$ at 2.5 GPa. **d**, Rietveld refinement of XRD pattern of $La_4Ni_3O_{10-\delta}$ at 34.0 GPa. The refinement parameters are summarized in Supplementary Table 3.

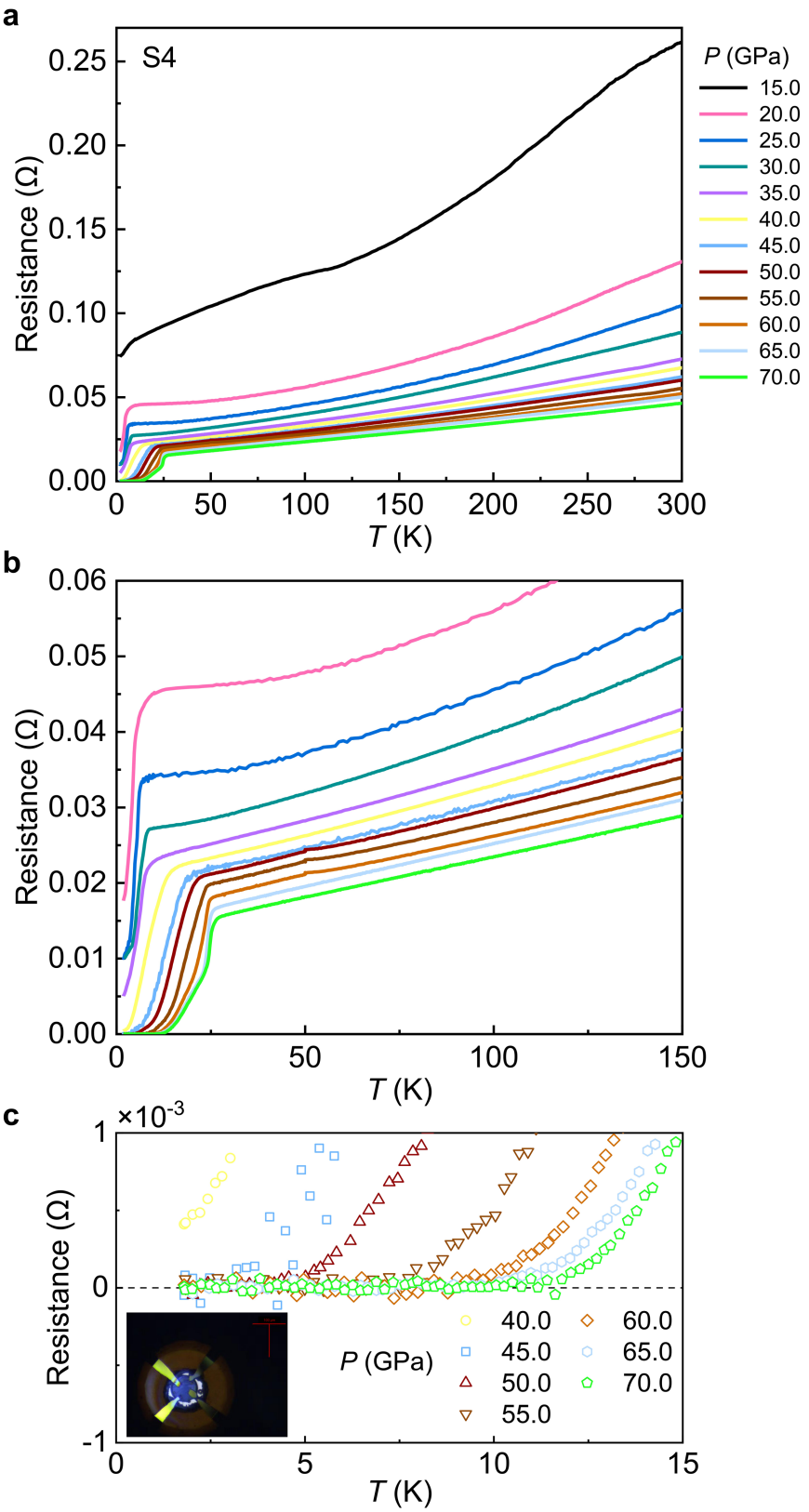

Extended Data Fig. 4 | Temperature-dependent resistances of sample 4 (S4) in a helium DAC. a, Temperature-dependent resistances of S4 under various pressures between 2 K and 300 K. **b**, Detailed resistance profile from 2 K to 150 K. Zero resistance below T_c is observed above 45 GPa. **c**, An enlarged view of the resistance curve below T_c, providing a closer examination of the zero-resistance state. The inset is a photograph depicting the electrodes used for the measurement.

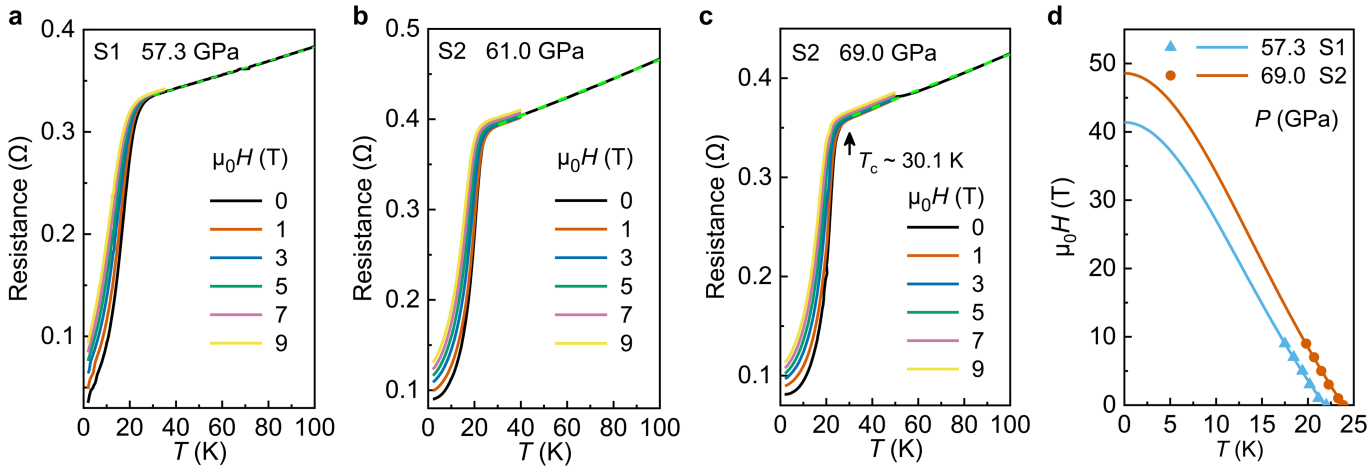

Extended Data Fig. 5 | Magnetic field effects on the superconducting transition in $La_4Ni_3O_{10-\delta}$ in a KBr DAC. a, Field dependences of electrical resistance at 57.3 GPa for sample S1. **b**, Field dependences of electrical resistance at 61.0 GPa for sample S2. **c**, Field dependences of electrical resistance at 69.0 GPa for sample S2. The green dashed lines depict the linear fit of the normal state resistances. **d**, The Ginzburg–Landau fittings of the upper critical fields at 57.3 (S1) and 69.0 GPa (S2). The magnetic fields are applied perpendicular to the *ab* plane.

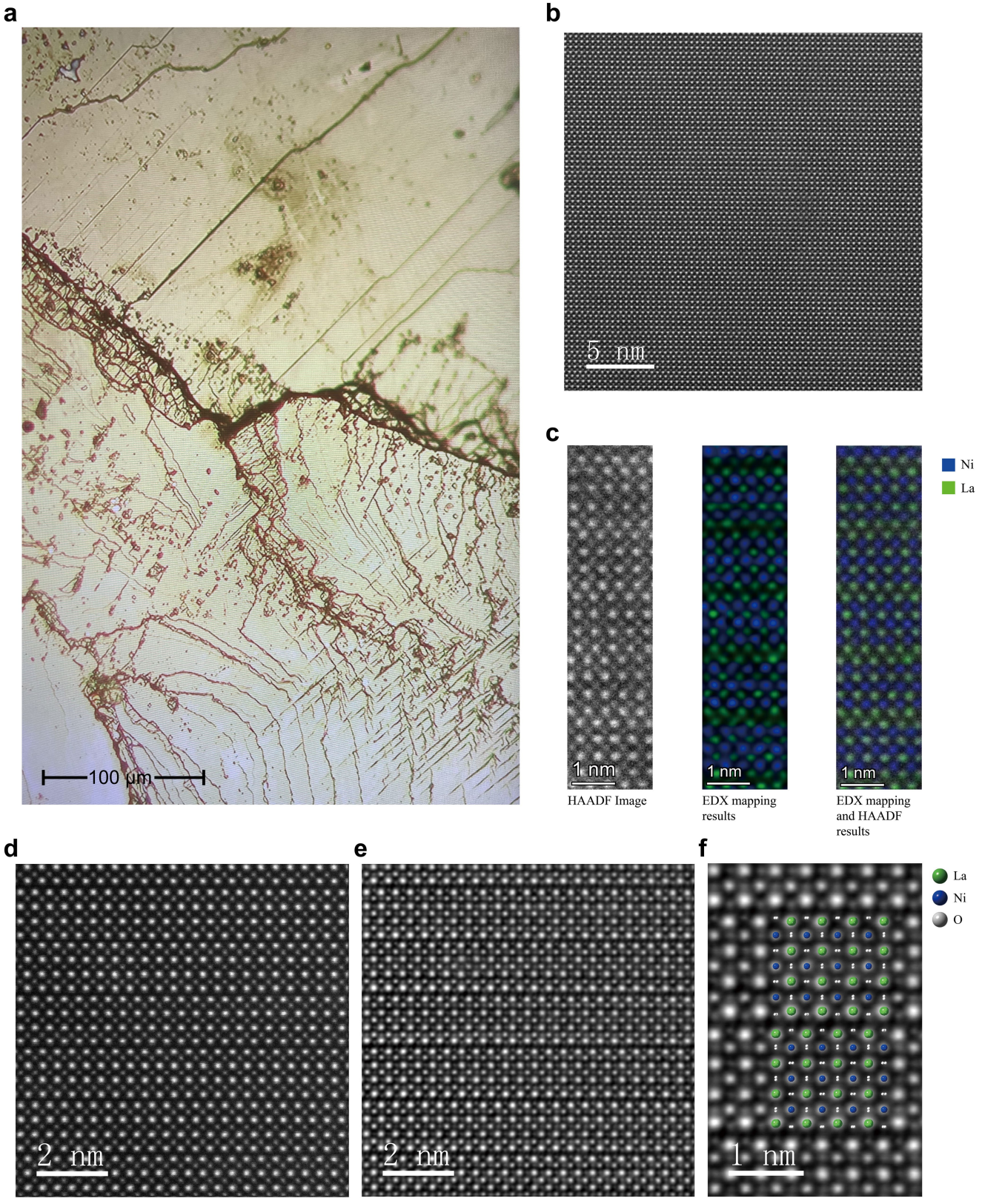

Extended Data Fig. 6 | STEM-HAADF and integrated differential phase contrast (iDPC) measurements of $La_4Ni_3O_{10-\delta}$ crystals. a, The cleavage plane of a $La_4Ni_3O_{10-\delta}$ single crystal. **b**, The STEM-HAADF image of a $La_4Ni_3O_{10-\delta}$ crystal along the [110] direction on the scale of 5 nm. **c**, Atomic EDX mapping results and STEM-HAADF image in the same region. **d**, The STEM-HAADF image of $La_4Ni_3O_{10-\delta}$ sample along the [110] direction on the scale of 2 nm. **e**, iDPC result in the same region and **f**, an enlarged view of the iDPC image. The oxygen atoms are clearly revealed through the iDPC imaging, aligning well with the crystal structure of $La_4Ni_3O_{10-\delta}$ determined by neutron diffraction and XRD measurements.

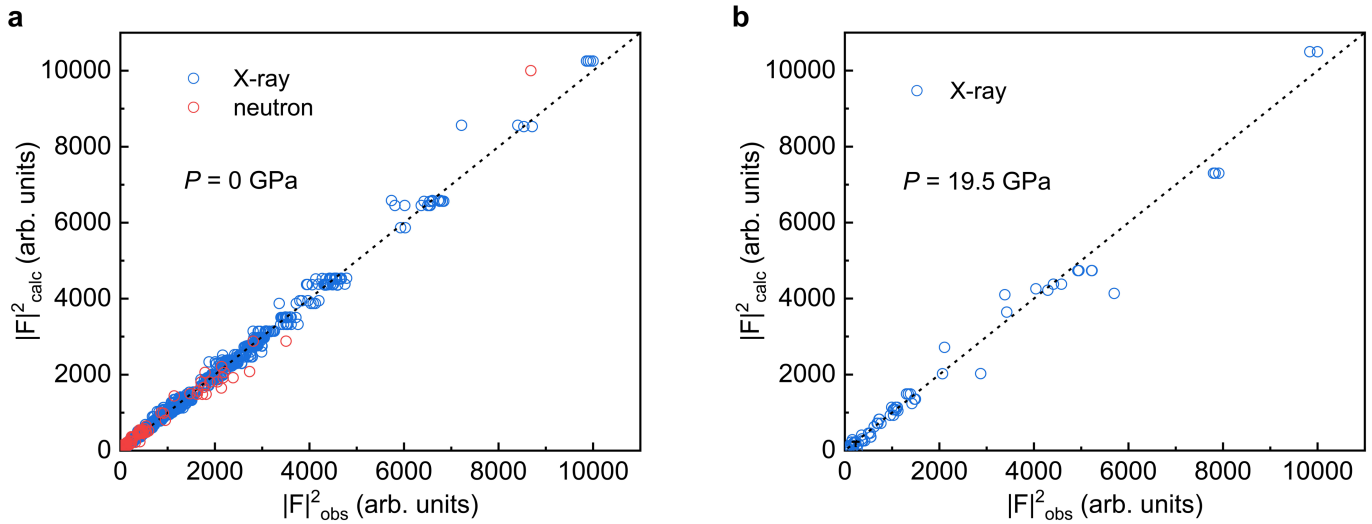

Extended Data Fig. 7 | Single-crystal refinements using neutron and X-ray diffraction data for $La_4Ni_3O_{10-\delta}$. **a**, Combined single-crystal refinement results using neutron and X-ray diffraction data for $La_4Ni_3O_{10-\delta}$. The integrated intensities of Bragg reflections from a $La_4Ni_3O_{10-\delta}$ single crystal, collected at room temperature and ambient pressure, are plotted against their calculated counterparts. Details of the refined parameters are provided in Supplementary Table 1. **b**, Single-crystal refinements of X-ray diffraction data. Integrated intensities of the Bragg reflections collected on a $La_4Ni_3O_{10-\delta}$ single crystal at room temperature and 19.5 GPa are plotted against their calculated counterparts. The refinement parameters are summarized in Supplementary Table 2. The refinements suggest a structural phase transition from monoclinic $P2_1/a$ to tetragonal $I4/mmm$ in $La_4Ni_3O_{10-\delta}$ under pressure.

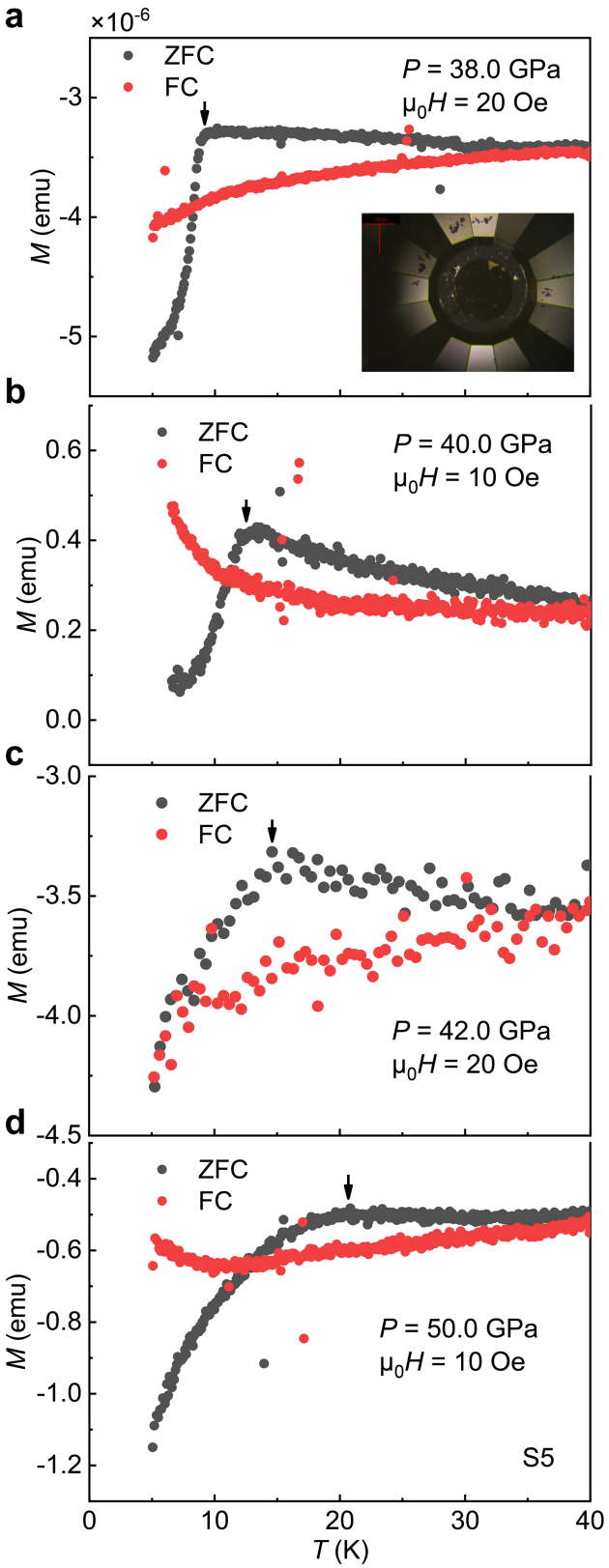

Extended Data Fig. 8 | Temperature-dependent d.c. susceptibilities of sample 5 (S5) under various pressures. a, Temperature dependent magnetization curves at 38.0 GPa under a magnetic field of 20 Oe applied perpendicular to the *ab* plane using the zero-field-cooled (ZFC) and field-cooled (FC) modes. The inset shows the photo of the crystal in the nitrogen mini-DAC. **b**, 40.0 GPa and 10 Oe. **c**, 42.0 GPa and 20 Oe. **d**, 50.0 GPa and 10 Oe. The black arrows indicate the superconducting transition temperatures. The broadening of the superconducting transition with increasing pressure could be attributed to the gradual deterioration of hydrostaticity in the nitrogen pressure-transmitting medium. This broadening is less pronounced in a smaller sample (S6), which contains more pressure-transmitting medium and, consequently, exhibits improved hydrostaticity (Fig. 3f–i).

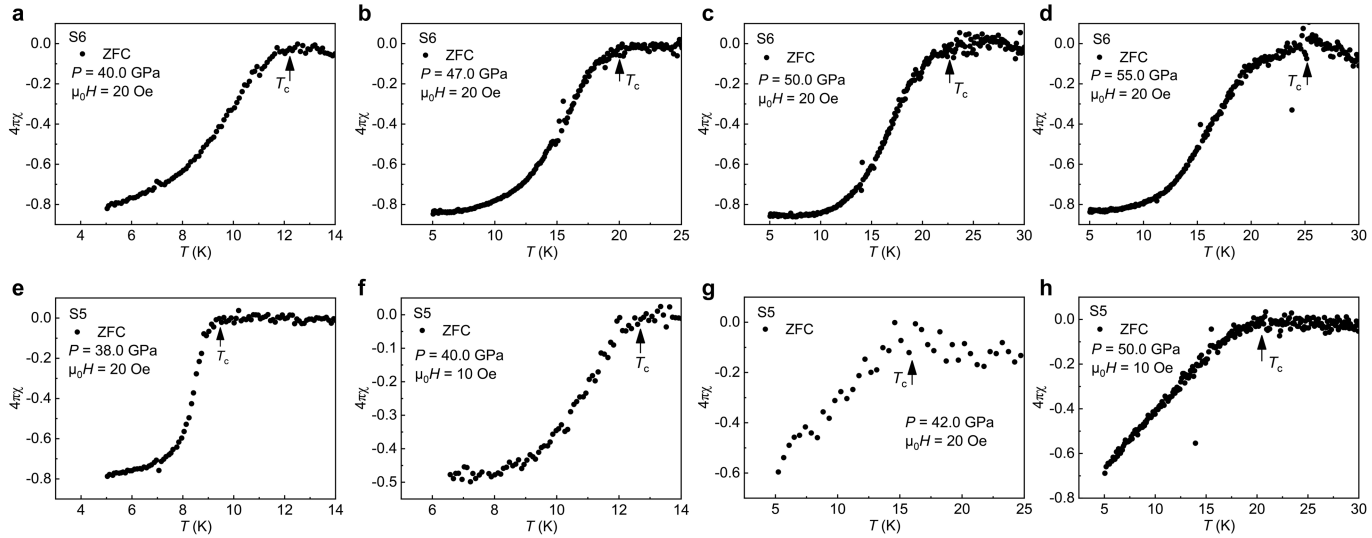

Extended Data Fig. 9 | Temperature dependent superconducting volume fractions of $La_4Ni_3O_{10-\delta}$ single crystals determined through d.c. susceptibility measurements in Fig. 3 (S6) and Extended Data Fig. 8 (S5). Superconducting volume fractions for S6 under **a**, 40.0 GPa; **b**, 47.0 GPa; **c**, 50.0 GPa; **d**, 55.0 GPa. Superconducting volume fractions for S5 under **e**, 38.0 GPa; **f**, 40.0 GPa; **g**, 42.0 GPa; **h**, 50.0 GPa.

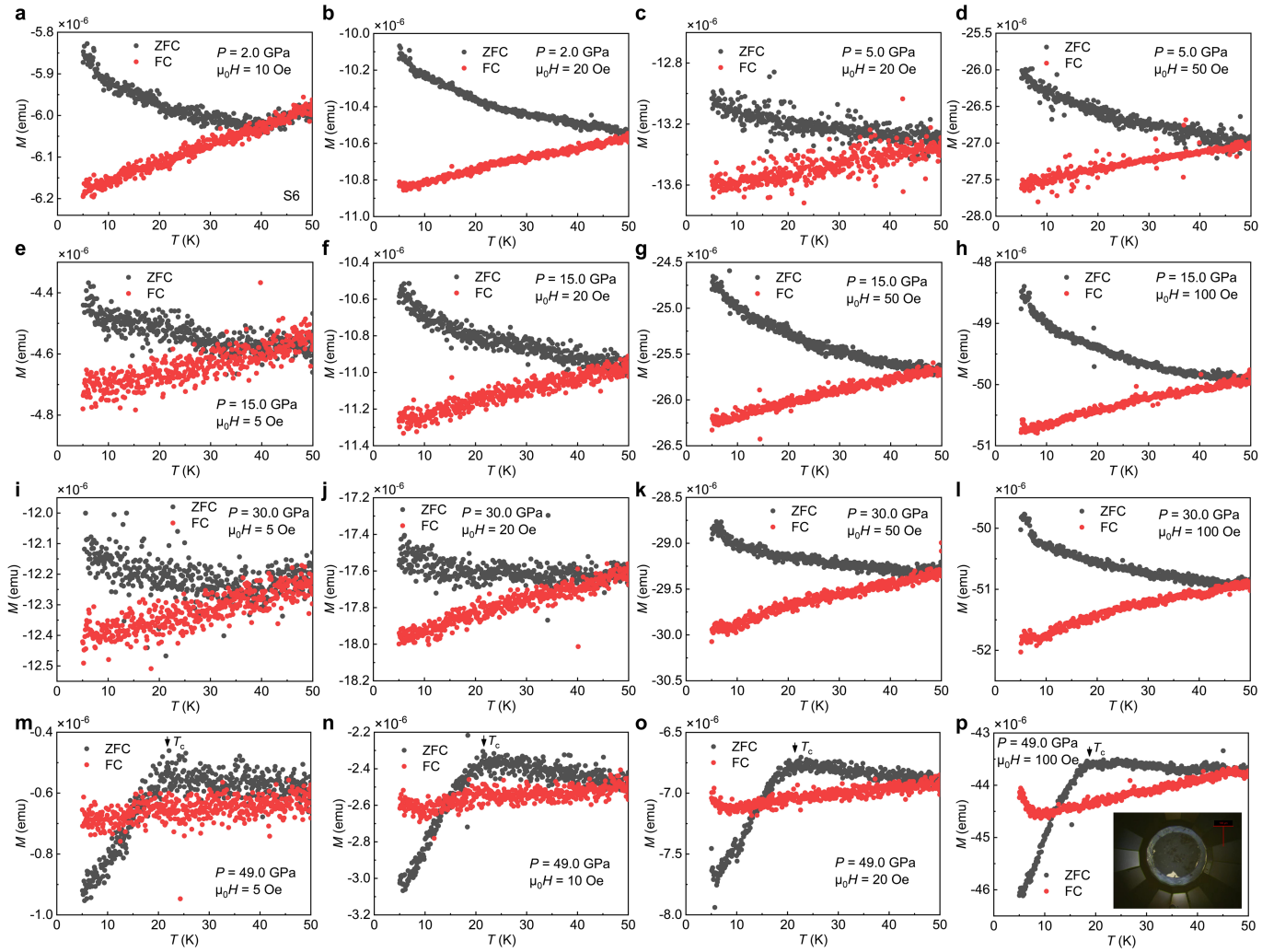

Extended Data Fig. 10 | Temperature-dependent magnetization curves of sample 7 (S7) under various pressures under a magnetic field applied perpendicular to the *ab* plane using the zero-field-cooled (ZFC) and field-cooled (FC) modes. a, 2.0 GPa and10 Oe **b**, 2.0 GPa 20 Oe. Temperature dependent magnetization curves at 5.0 GPa under magnetic fields of **c**, 5.0 GPa and 20 Oe and **d**, 5.0 GPa and 50 Oe. **e**, 15.0 GPa and 5 Oe; **f**, 15.0 GPa and 20 Oe; **g**, 15.0 GPa and 50 Oe; **h**, 15.0 GPa and 100 Oe. **i**, 30.0 GPa and 5 Oe; **j**, 30.0 GPa and 20 Oe; **k**, 30.0 GPa and 50 Oe; **l**, 30.0 GPa and 100 Oe. **m**, 49.0 GPa and 5 Oe; **n**, 49.0 GPa and 10 Oe; **o**, 49.0 GPa and 20 Oe; **p**, 49.0 GPa and 100 Oe. The inset shows the photo of the crystal in the mini-DAC.